

# Lumley decomposition of turbulent boundary layer at high Reynolds numbers

Murat Tutkun<sup>1,2,\*</sup> and William K. George<sup>3</sup>

<sup>1</sup>*Institute for Energy Technology, Department of Process and Flow Technology, Kjeller, Norway*

<sup>2</sup>*University of Oslo, Department of Mathematics, Blindern, Oslo, Norway*

<sup>3</sup>*Imperial College London, Department of Aeronautics, London SW7 2AZ, United Kingdom*

(Dated: October 18, 2016)

## Abstract

The decomposition proposed by Lumley in 1966 is applied to a high Reynolds number turbulent boundary layer. The experimental database was created by a hot-wire rake of 143 probes in the LML wind tunnel. The Reynolds numbers based on momentum thickness ( $Re_\theta$ ) are 9800 and 19 100. Three-dimensional decomposition is performed; namely proper orthogonal decomposition (POD) in the inhomogeneous and bounded wall-normal direction, Fourier decomposition in the homogeneous spanwise direction and Fourier decomposition in time. The first POD modes in both cases carry nearly 50% of turbulence kinetic energy when the energy is integrated over Fourier dimensions. The eigenspectra always peak near zero frequency and most of the large scale, energy carrying features are found at the low end of the spectra. The spanwise Fourier mode which has the largest amount of energy is the first spanwise mode and its symmetrical pair. Pre-multiplied eigenspectra have only one distinct peak and it matches the secondary peak observed in the log-layer of pre-multiplied velocity spectra. Energy carrying modes obtained from the POD scale with outer scaling parameters. Full or partial reconstruction of turbulent velocity signal based only on energetic modes or non-energetic modes revealed the behaviour of  $u_{\text{rms}}$  in distinct regions across the boundary layer. When  $u_{\text{rms}}$  is based on energetic construction, there exists (a) an exponential decay from near wall to log-layer, (b) a constant layer through the log-layer and (c) another exponential decay in outer region. The non-energetic construction reveals that  $u_{\text{rms}}$  has (a) an exponential decay from the near-wall to the end of log-layer, and (b) a constant layer in outer region. Scaling of  $u_{\text{rms}}$  using the outer parameters is best when both energetic and non-energetic profiles are combined.

## I. INTRODUCTION

Lumley<sup>1</sup> introduced the idea of an optimal projection based on energy into the field of turbulence as a quantitative and unbiased method of identifying and studying the large scale energy containing features in turbulent fields. For fields of finite total energy, solutions to Lumley's integral equation are proper and orthogonal, hence the term POD emerges. And this term is often used (incorrectly) to describe the more general solutions to his integral equation which will be applied herein.

The general Lumley decomposition provides an optimum deterministic description of the field, the so-called eigenvalues and eigenfunctions (or eigenmodes). These are the solutions obtained by seeking the largest projection onto the stochastic velocity field of turbulence in a mean square sense. Maximization of the projection results in an integral value problem, the Lumley integral equation<sup>2</sup> for which the kernel is the two-point cross-correlation tensor of the velocity field. Deterministic description of the field provided by the Lumley decomposition has been found to be very efficient at extracting the most energetic modes of the flow and ordering them according to their energy content<sup>3-10</sup>.

Even though the Lumley decomposition was introduced as an optimal and a mathematical way of breaking different scales of turbulent motion apart, utilization of the method took some time, mainly due to difficulties associated with the measurement and computation of the two-point cross-correlations tensor. As pointed out by George<sup>11</sup>, it needs sufficient information on the two-point cross-correlation tensor so that a complete space-time realization of the turbulence velocity field can be obtained. Computation of the statistically converged cross-correlation tensor from the measured velocities with sufficient information is difficult in terms of computing power and speed capabilities, even now and especially was a serious limitation a few decades ago.

The first partially successful experimental implementation was for pipe flow<sup>12</sup>, and used only the inhomogeneous direction perpendicular to the wall for a POD decomposition. However, it was almost two decades after Lumley's proposal<sup>1</sup> that the full potential began to be realized in the 1980s for high Reynolds number axisymmetric mixing layer<sup>3,4,13,14</sup> and for low Reynolds number pipe flow<sup>15</sup>. Since then, experimental utilization of various partial decompositions have been widely used to decompose the turbulent flows into different scales of motion. Moin and

Moser<sup>16</sup> applied the POD on a database created by the direct numerical simulation (DNS) of low Reynolds number turbulent channel flow and extracted the most energetic characteristic scales of turbulence.

One of the most striking features of the POD is its ability to describe the energetic large scale features with only a few eigenmodes in an optimal manner, especially if the flow is first decomposed into its Fourier modes in the periodic or homogeneous directions. Free shear turbulent flows have been investigated extensively using the combined Fourier-POD technique<sup>3-10,17-20</sup>. Glauser<sup>14</sup> showed that the orthogonal decomposition was very efficient in organizing the large scale structures in the axisymmetric mixing layer. The first POD mode contained 40% of the total turbulence kinetic energy. The energy content of the first three POD modes was about 80% in total. These initial results were based on measurements using hot-wire rakes of single wire probes. The capability of the POD to capture most of the turbulence kinetic energy by a few orthogonal eigenmodes led a number of research groups to apply this technique, initially to canonical flows, but later to flows in more complex geometries<sup>21,22</sup>.

By contrast to the amount of research conducted using the POD in turbulent free shear flows (mainly experimental), there have been only a limited number of applications carried out for the wall bounded flows, and these are reviewed in the next section below. This is mainly because of the experimental difficulties in such flows imposed by the required number of hot-wire rakes of many probes, or the statistical convergence problem of numerical simulations. With the advent of hardware and software developments, particle image velocimetry (PIV), which provides three-dimensional velocity information on a plane, has recently become a very useful tool in measurements of the two-point cross-correlation with very high spatial resolution. These have been used for channel flow<sup>23</sup>, pipe flow<sup>24</sup> and flume<sup>25</sup> experiments to be able to perform the POD analysis on the obtained data. Numerical studies which can be found in the literature are also primarily for the channel flow simulations. There has been no research analyzing high Reynolds number turbulent boundary layers using the powerful features of the classical POD. Therefore, our work described in this paper is unique.

As it is clear from above discussions, the combined Fourier-POD is very efficient in capturing the maximum amount of turbulence kinetic energy with minimum number of modes, at least if the field is of finite total energy and limited extent. We therefore implement this methodology

to analyze the velocity measurements of the streamwise component of high Reynolds number zero pressure gradient turbulent boundary layer data obtained by using a hot-wire rake of 143 single wire probes.

Our data set and analyzes are different from the previous research conducted on the wall bounded flows: first because it is a high Reynolds number turbulent boundary layer flow, and second because it is of very large extent so that a large probe array could be utilized. In the sections following the historical review, the background theory and implementation of the method are discussed. Then the eigenspectra and turbulence kinetic energy distributions from the POD analysis are presented. Finally, the instantaneously measured streamwise velocity fluctuations are projected back onto the empirical eigenfunctions in order to reconstruct the velocity field, and break it into its different scales of motions.

## II. HISTORICAL REVIEW

The first POD application on the wall bounded flows by Bakewell and Lumley<sup>12</sup> investigated the near wall region of turbulent pipe flow up to  $y^+$  of 40. The Reynolds number based on the pipe diameter was 8700, and glycerine was used as working fluid to be able to study the viscous sublayer near the wall. Hot-film anemometers were employed for the measurements of streamwise velocity fluctuations only along a single line perpendicular to the wall. They inferred the most dominant large scale structure of the flow using mixing length theory and the continuity equation. They were only able to obtain the first eigenmode because of the inaccuracy of the measured two-point space-time correlations. Later, in a subsequent experiment in the same facility, Herzog<sup>15</sup> measured two components of the velocity, namely the azimuthal and the streamwise components. The missing five members of the cross-correlation tensor were obtained utilizing the general symmetry properties in connection with the continuity equation. The measurement grid was established using six points in wall-normal direction up to  $y^+$  of 40, seven points in the streamwise direction of to  $x^+$  of 49, six points in the azimuthal direction up to  $z^+$  of 136. He reported that the most dominant mode contained 50% or more of the kinetic energy due to streamwise velocity component, and first three POD modes contained more than 90% of the turbulence kinetic energy because of the streamwise fluctuations.

Following these experimental studies, the most detailed POD study in the wall bounded

turbulence came from Moin and Moser<sup>16</sup> and they studied a database of direct numerical simulation of turbulent channel flow using both scalar and vectorial decompositions in one or more dimensions. The Reynolds number based on the friction velocity and half channel height was 180, corresponding to the Reynolds number of 3200 based on centerline mean velocity and half channel height. They were able to show that the energy carried by the first eigenmode, regardless of the number of dimension included in the analysis, was 30-50% of the total turbulence kinetic energy when the half channel was taken into account. The contribution of the first three POD modes changed from 50% to 75% depending on the number of dimensions. They also used shot-noise decomposition and were able to extract the most dominant characteristic eddy, which had 76% of the total turbulence kinetic energy.

Liu et al.<sup>23,26</sup> studied the turbulent channel flow by experimental utilization of the POD method. One of the Reynolds numbers tested was much higher than the previous investigations listed above, i.e., 5378 and 29 935 when computed using bulk velocity and the channel height. PIV was used as an experimental tool with high spatial resolution to measure the two components of turbulent velocity field, namely streamwise and wall-normal components. The first study<sup>23</sup> focused on the similarity of the eigenspectra and eigenfunctions in the outer layer of the turbulent channel flow, and showed that the proper scaling of the eigenspectra using the friction velocity and outer length scale results in a collapse in the eigenspectra. The second paper<sup>26</sup> was more thorough and did detailed analyzes on the energy and Reynolds stress distribution over different eigenfunctions. For both of the Reynolds numbers investigated, they reported that the energies of first 6 and 12 eigenmodes were approximately 35 and 50% of the total turbulence kinetic energy respectively. They also noted the Reynolds stresses due to these 6 and 12 eigenmodes were approximately 50% and 70% of the total Reynolds stress within the domain respectively. The large scale motions of turbulence represented by the low eigenmodes with high turbulence kinetic energy had wavelengths longer than three times the half channel height.

Bailey and Smits<sup>27</sup> used the POD and azimuthal Fourier modes to investigate large- and very large-scale motions in turbulent pipe flow at Reynolds number of  $1.5 \times 10^5$ , which was based on the pipe diameter and area-averaged velocity across the cross-section. The measurements were conducted using a pair of single sensor hot-wire probes sampling at different radial and

azimuthal positions to be able to obtain the cross-correlations. The first POD mode in this case carried about 75% of turbulence kinetic energy. Because of the periodicity of the flow in the azimuthal direction, Fourier series expansion was possible. As shown in the paper, they found the azimuthal mode number 3 to be the most dominant mode. They also observed no clear separation in eigenspectra for large and very large scale motions as present in pre-multiplied one-dimensional wavenumber spectra. Following this, Hellström and Smits<sup>24</sup> and Hellström et al.<sup>28</sup> used snapshot POD and investigated structures of turbulent pipe flow, focusing in particular to attached eddies and large scale motions. In a recent study, Baltzer et al.<sup>29</sup> investigated large and very large scales of motion using DNS of a fully developed incompressible turbulent pipe flow at Reynolds number, based on bulk velocity and pipe diameter, of 24580. They performed POD analysis in order to identify the most energetic modes and to describe the structural organization in the flow. In particular, they showed the relation between roll cells, very large helical scales and elongated streaks to particular POD modes.

Our study, by contrast with those described above, utilizes the full three-dimensional 'slice-POD' utilized by Citriniti and George<sup>5</sup>. Only the streamwise dimension is missing (since the downstream position was fixed). But, because of the relatively low turbulence intensity, the time-dimension is more representative of streamwise spatial variations. To avoid confusion with Taylor's hypothesis interpretations, we have presented the time data in frequency space. Recently George<sup>2</sup> has raised concerns about whether any missing dimension aliases information into the eigenfunctions in the other directions. We have tried to point out where this may be the case.

### III. EXPERIMENTAL SETUP

The experimental database used for the proper orthogonal decomposition analysis in this paper has previously been documented in detail by Tutkun et al.<sup>30,31</sup> and Coudert et al.<sup>32</sup>. Therefore, here we only present a summary of the experimental setup and flow characteristics.

The Laboratoire de Mécanique de Lille (LML) wind tunnel was used to measure the turbulent boundary layer at high Reynolds numbers. Measurements were carried out using a hot-wire rake of 143 single-wire probes. The test section has a constant cross-section area and its dimensions are 21.6 m in length, 2 m in width and 1 m in height. A detailed description of the wind tunnel



FIG. 1. Hot-wire rake of 143 probes in the LML wind tunnel.

together with its basic flow characteristics are documented in papers published by Stanislas and his group<sup>33,34</sup>.

Two Reynolds numbers, achieved by only changing the freestream velocity, were tested over a flat plate (the bottom wall of the tunnel). The Reynolds numbers based on momentum thickness,  $Re_\theta = U_\infty \theta / \nu$ , were 9800 and 19100 for freestream velocities ( $U_\infty$ ) of  $5 \text{ m s}^{-1}$  and  $10 \text{ m s}^{-1}$  respectively. The boundary layer thicknesses,  $\delta$ , at the measurement location, which was 18 m downstream of the entrance of test section, were 0.30 m and 0.32 m at Reynolds numbers of 19100 and 9800 respectively. The friction velocities were measured using a micro-PIV system, and  $u_\tau$  were  $0.354 \text{ m s}^{-1}$  and  $0.183 \text{ m s}^{-1}$  at high and low Reynolds numbers respectively. This results in approximately equal  $u_\tau / U_\infty$  for the Reynolds numbers tested in this study.

The hot wire rake used in this investigation is shown in figure 1. The main purpose of measuring the turbulent boundary layer using an array of hot-wire probes was to obtain both spatial and temporal information about the flow simultaneously. The rake covered an area of approximately  $30 \times 30 \text{ cm}^2$  perpendicular to the streamwise direction. The probes were distributed over 13 vertical combs, which were staggered in the spanwise direction symmetrically around the center comb. The center comb was located in the middle of spanwise width of the tunnel and therefore corresponded to  $z=0$ . The symmetric pairs of the vertical combs were distributed at  $\pm 4 \text{ mm}$ ,  $\pm 12 \text{ mm}$ ,  $\pm 28 \text{ mm}$ ,  $\pm 60 \text{ mm}$ ,  $\pm 100 \text{ mm}$  and  $\pm 140 \text{ mm}$ . Each of these

vertical combs carried 11 hot wire probe sensors in total. The spacing between the probes in wall-normal direction was logarithmic. Position of the probes with respect to the wall ( $y=0$ ) were 0.3 mm, 0.9 mm, 2.1 mm, 4.5 mm, 9.3 mm, 18.9 mm, 38.1 mm, 76.5 mm, 153.3 mm, 230.1 and 306.9 mm. Therefore, the closest point of measurement at the wall corresponded to  $y^+$  of 3.7 and 7 for Reynolds numbers of 9800 and 19 100 respectively. The coordinate points listed above are essentially the coordinates the rake was designed for. However, there were some manufacturing imperfections at the probe locations in the wall-normal direction, particularly in the vicinity of the wall. Therefore, the precise location of each probe were found by illuminating the tips of the probes using a laser sheet and taking a picture of the rake (or the tips of the probes) using two high resolution, overlapping cameras ( $1376 \times 1040$  pixels with pixel size of  $6.7 \mu\text{m}$ ). The uncertainty in finding the precise location of the probes was 0.03 mm with a 95% confidence level.

Detailed analysis of the blockage introduced by the rake was carried out and published by Coudert et al<sup>32</sup>. They performed a series of careful measurements of the flow both with and without the hot-wire rake in place in the wind tunnel. They observed that the disturbance caused by the rake only affected the mean velocity field, whereas the turbulence statistics were unaffected. Therefore, they concluded that the blockage at both velocities was a potential flow disturbance which was further verified quantitatively by a model based on complex potential. The model shows that the blockage is only on the mean velocity field. Further comparison between the disturbed and undisturbed fields using both single-point and two-point turbulence statistics also supported this.

The probes were in-house developed by Laboratoire d'Etudes Aérodynamiques, Université de Poitiers, UMR CNRS 6609, ENSMA. The sensing elements were 0.5 mm in length,  $\ell$ , and  $0.25 \mu\text{m}$  in diameter,  $d$ , corresponding to wire length and diameter in wall units,  $\ell^+$  ( $= \ell u_\tau / \nu$ ) and  $d^+$  ( $= d u_\tau / \nu$ ) of 11.8 and 0.006 for  $\text{Re}_\theta$  of 19 100, and 6.1 and 0.003 for  $\text{Re}_\theta$  of 9800 respectively. The vertical combs were made of 1.8 mm thick, double sided conventional circuit boards. This method for constructing hot-wire rakes of many probes was previously used for multi-point measurement in turbulent flows<sup>14,17,18</sup>.

The probes on the hot wire rake were operated using an in-house developed, multi-channel, constant temperature anemometer (CTA) system. More details on the design and performance

of the system were documented by Woodward<sup>35</sup>. The same system was used extensively to perform multi-point hot wire measurements<sup>5-7</sup> because of its capability of measuring the spectra and related statistics with a very low noise-to-signal ratio, no thermal drift over time and no cross-talk between the channels<sup>36</sup>.

During the experiments the hot-wire anemometer output voltages from 143 channels together with tunnel temperature, tunnel dynamic pressure and synchronization signal for the anemometry system were recorded at 30 kHz simultaneously for 6 seconds long blocks, corresponding to sampling interval in wall units ( $\Delta t^+$ ) of  $\sim 0.27$  at  $Re_\theta$  of 19 100 and that of  $\sim 0.07$  at  $Re_\theta$  of 9800 (where  $\Delta t^+ = \Delta t u_\tau^2 / \nu$ ). Since this study focuses on energetic modes of the turbulent boundary layer which are on the low end of the frequency (or wavenumber) domain, we utilized a low-pass digital filter to remove any possible high frequency noise seen in the spectra. The digital filter, a 9<sup>th</sup> order Butterworth filter, was designed using Matlab signal processing toolbox and the cut-off frequency was set at 3 kHz of high Reynolds number case and 1.5 kHz for low Reynolds number case, because most of our interest lies up to only a few hundred Hertz.

#### IV. EXPERIMENTAL IMPLEMENTATION OF THE POD

##### A. Formulation of the POD for Turbulent Boundary Layer

The full four dimensional representation of the Lumley integral<sup>37</sup> in a Cartesian coordinate system is given by:

$$\int_D R_{i,j}(x, x', y, y', z, z', t, t') \phi_j(x', y', z', t') dx' dy' dz' dt' = \lambda \phi_i(x, y, z, t) \quad (1)$$

where  $x, y, z$  and  $t$  denote coordinates in streamwise, wall-normal and spanwise directions and time respectively. The prime ( $'$ ) represents a different position in space and time. The kernel of the equation, which is the two-point cross-correlation tensor, can be written as:

$$R_{i,j}(x, x', y, y', z, z', t, t') = \langle u_i(x, y, z, t) u_j(x', y', z', t') \rangle \quad (2)$$

where the subscripts  $i$  and  $j$  are indices and represent appropriate velocity components. Because

the statistically two-dimensional turbulent boundary layer is stationary in time and homogeneous in the spanwise direction, the two-point cross-correlation tensor reduces to only a function of separations in spanwise direction and time:

$$\tilde{R}_{i,j}(x, x', y, y', \Delta z, \tau) = R_{i,j}(x, x', y, y', z, z', t, t') \quad (3)$$

where  $\Delta z = z' - z$  and  $\tau = t' - t$ . Since the Lumley integral reduces to harmonic decompositions in the homogenous and stationary directions, these directions can be removed by taking the Fourier transform of the two-point cross-correlation tensor given in equation (3). Fourier transformation in time,  $t$ , and the homogeneous direction,  $z$ , yields the two-point cross-spectral tensor:

$$S_{i,j}(x, x'; y, y'; k; f) = \frac{1}{2\pi} \int_{-\infty}^{\infty} \int_{-\infty}^{\infty} \tilde{R}_{i,j}(x, x'; y, y', \Delta z, \tau) e^{-i(2\pi f\tau + k\Delta z)} d\tau d(\Delta z) \quad (4)$$

where  $f$  is the frequency corresponding to  $\tau$  and  $k$  is the spanwise Fourier mode number corresponding to  $\Delta z$ .

Since only one downstream location is considered as in this paper, the streamwise dependence of the two-point cross-spectral tensor in equation (4) can be treated as a parameter. The resulting POD integral equation has been called the slice-POD<sup>3,5,6,8,10,19</sup>. The slice POD equation in our study can be written as:

$$\int_{y'} S_{i,j}(y, y'; k; f) \phi_j^*(y'; k; f) dy' = \lambda(k; f) \phi_i(y; k; f) \quad (5)$$

where  $\lambda(k; f)$  and  $\phi_i(y; k; f)$  represent the eigenspectra and eigenfunctions for each spanwise mode and frequency, respectively. Since the integration is performed over the wall-normal coordinate direction, the domain is bounded by the boundary layer thickness,  $\delta$ ; hence it is of finite total energy and truly a POD integral.

As detailed in many other sources<sup>1,11,38</sup>, if the field of interest is bounded and of finite energy, then the Hilbert-Schmidt theory applies. Solution of the integral equation given in equation (5) in the domain of finite energy produces denumerably many solutions ( $\phi_i$ s in this case) instead of a single solution. There is a pair of  $\lambda$  (eigenvalue) and  $\phi_i$  (eigenfunction) for each of these denumerable solutions. Therefore, equation (5) can be written as:

$$\int_{y'} S_{i,j}(y, y'; k; f) \phi_j^{*(n)}(y'; k; f) dy' = \lambda^{(n)}(k; f) \phi_i^{(n)}(y; k; f) \quad (6)$$

where  $n = 1, 2, 3, \dots$  and represents the solution index, or POD mode number.

## B. Reconstruction of the Velocity Field

It is possible to reconstruct the instantaneous velocity field of turbulence using the deterministic POD eigenmodes together with their random coefficients, which are obtained by projecting the velocity field onto the deterministic eigenmodes. Only the streamwise velocity component can be reconstructed in our study. Since the kernel,  $S_{1,1}(y, y'; k; f)$ , is written as a function of spanwise Fourier mode number,  $k$ , and frequency,  $f$ , the resulting eigenfunctions and eigenvalues are also functions of these two parameters as described in the previous sections. Therefore, reconstruction of the velocity field begins by finding the random coefficients,  $a_{(n)}(k, f)$ , by projecting the eigenfunctions onto the doubly Fourier transformed velocity fluctuations as follows:

$$a_{(n)}(k, f) = \int_0^\infty \hat{u}(y, k, f) \phi^{(n)*}(y, k, f) dy \quad (7)$$

where the integration is performed in the inhomogeneous wall-normal direction using the trapezoidal rule. The upper limit of integration is replaced by the boundary layer thickness,  $\delta$ . The fluctuating velocity is transformed into the Fourier domain, first in time and second in the homogeneous spanwise direction to obtain  $\hat{u}(y, k, f)$ ; i.e.,

$$\hat{u}(y, k, f) = \int_{-\infty}^\infty \int_{-\infty}^\infty u(y, z, t) e^{-i(2\pi ft + kz)} dz dt \quad (8)$$

The experimental utilization of the second Fourier transformation in the spanwise direction is rather difficult because of the nonuniform grid of hot-wire rake probes as detailed in the experimental setup chapter. To be able to perform the second Fourier transformation in  $z$ , linear interpolation of the fluctuating velocities at each constant wall-normal location is performed by the smallest increment available in  $z$ -direction. In this way, a uniform grid spaced by 4 mm is created and subsequent Fourier transformation is applied on this grid. Note that construction of the kernel,  $S_{1,1}(y, y'; \Delta z; f)$ , (and the resulting eigenfunctions and eigenvalues) are already on a uniformly spaced grid of 4 mm, because it is possible to create this grid size using different

vertical combs in connection with the homogeneity of the statistical quantities in the spanwise direction.

The doubly Fourier transformed streamwise component of fluctuating velocities are obtained as a linear combination of eigenfunction using the random coefficients obtained by equation (7):

$$\hat{u}_{rec}(y, k, f) = \sum_{n=1}^N a_{(n)}(k, f) \phi^{(n)*}(y, k, f) \quad (9)$$

where subscript '*rec*' stands for "reconstructed". The reconstructed velocity expressed in terms of spanwise Fourier modes and frequency can be mapped back into real space in two steps:

(i) Inverse Fourier transformation in frequency:

$$\hat{u}_{rec}(y, k, t) = \int_{-\infty}^{\infty} \hat{u}_{rec}(y, k, f) e^{i2\pi ft} df \quad (10)$$

(ii) Inverse Fourier transformation in spanwise Fourier index:

$$u_{rec}(y, z, t) = \int_{-\infty}^{\infty} \hat{u}_{rec}(y, k, t) e^{ik\Delta z} dk \quad (11)$$

The fluctuating velocity given by equation (11) can also be reconstructed using some subset of the POD and spanwise Fourier modes to investigate the dynamics associated with that subset of modes. This can be achieved by setting the random coefficients of all POD modes out of the subset of interest to zero, and following the same route from equation (8) to equation (11). If all POD and spanwise Fourier modes are used for the reconstruction, the original velocity signal can be recovered within the numerical accuracy. By selecting the most energetic POD and Fourier modes only, it is possible to study large scale, energy carrying motions of turbulence using the reduced velocity reconstruction which does not count the intermediate and small scales.

## V. RESULTS

The results presented here and in the rest of the paper are based on a one-component scalar proper orthogonal decomposition of streamwise component of the turbulent fluctuations, which was the only measured component during the experiments. Hereafter all reference to the proper orthogonal decomposition will mean the one-component scalar decomposition.

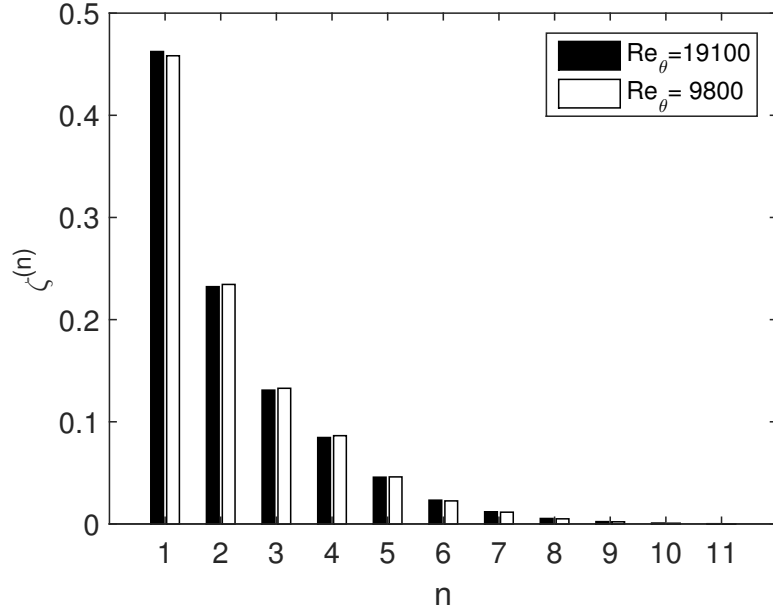


FIG. 2. Normalized eigenvalue distribution,  $\zeta^n$ , for each POD mode,  $n$ . (Note that these have been integrated over both frequency and wavenumber.)

### A. Eigenvalue Distribution over POD Modes

The eigenvalue distribution presented in figure 2 demonstrates that the POD is efficient and optimal in terms of capturing the largest amount of turbulence kinetic energy by the fewest modes. Each bar represents the normalized eigenvalues integrated over frequency and summed over the spanwise Fourier modes. The distribution of eigenvalues is computed as follows:

Percentage of turbulence kinetic energy		
	$Re_\theta = 19\ 100$	$Re_\theta = 9800$
$\lambda^{(1)}$	46	46
$\lambda^{(1)} + \lambda^{(2)}$	70	69
$\lambda^{(1)} + \lambda^{(2)} + \lambda^{(3)}$	83	83
$\lambda^{(1)} + \lambda^{(2)} + \lambda^{(3)} + \lambda^{(4)}$	91	91
$\lambda^{(1)} + \lambda^{(2)} + \lambda^{(3)} + \lambda^{(4)} + \lambda^{(5)}$	96	96

TABLE I. Percentage of turbulence kinetic energy captured by the POD modes.

$$\zeta^{(n)} = \frac{\sum_{k=1}^M \int_{-\infty}^{\infty} \lambda^{(n)}(k, f) df}{\sum_{n=1}^N \sum_{k=1}^M \int_{-\infty}^{\infty} \lambda^{(n)}(k, f) df} \quad (12)$$

where the denominator is the total turbulence kinetic energy at the plane normal to the stream-wise direction<sup>11,16</sup>.

Each bar in figure 2 indicates the contribution of the corresponding POD modes to the total turbulence kinetic energy of the domain. To within experimental error the results at two different Reynolds number are the same.

Table I presents the percentage of energy contribution of POD modes to the overall turbulence kinetic energy due to only streamwise velocity fluctuations. The results show that the first five POD modes contain more than 95% of the total energy. If the energy content of the first four POD modes is investigated, we see that approximately 91% of the total energy is carried by these three modes. Note that these normalized values are integrated and summed over frequency and spanwise Fourier modes. This means that each bar in figure 2 is comprised of 65 536 Fourier coefficients in the frequency domain and 71 harmonic modes in the Fourier domain corresponding to spanwise direction. Therefore one should always be careful when assessing a bar graph like figure 2 since it presents an integrated picture. Note that this is especially problematical for applications of the so-called 'snap-shot POD', since it mixes all the Fourier and POD modes together. (George<sup>2</sup> has discussed the implications of this, especially in Appendix 2. Note that all of the results of this paper use the 'classical POD' and we have avoided the 'snapshot POD' altogether.)

As shown in figure 2 and documented in table I, there is no measurable Reynolds number dependence. Partly this is because both experiments are at relatively high Reynolds numbers (at least compared to most). And the dominant contribution to the overall energy comes from the outer part of the boundary layer at these high Reynolds numbers. The two Reynolds number of this experiment,  $Re_{\theta}$  of 9800 and 19 100, correspond to  $\delta^+$  values of 3745 and 7250. So both  $\delta^+$  are at or above the threshold value of 3000 suggested by George and Castillo<sup>39</sup> (or GC97) for there to be a proper asymptotic outer flow and the beginning of a real overlap region. Below  $\delta^+$  of 3000 they expected the Reynolds number effects on the outer flow to be

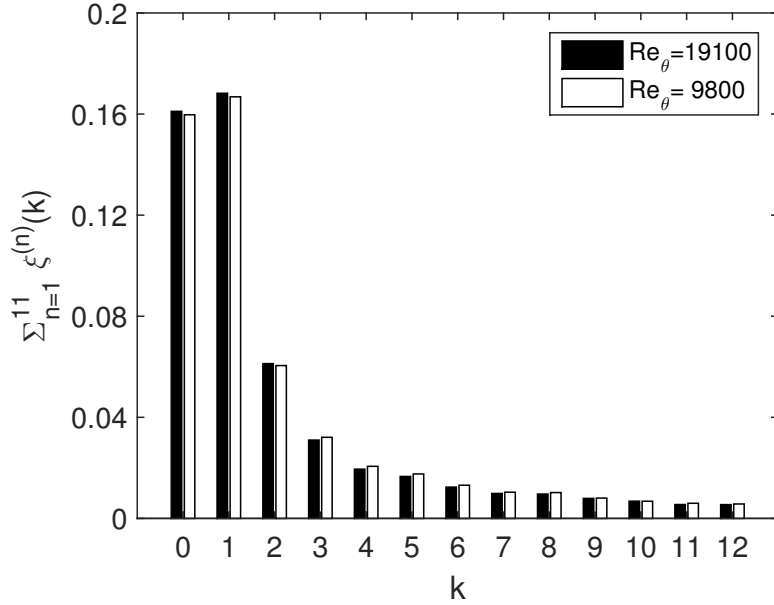


FIG. 3. Normalized eigenvalue distribution,  $\xi^{(n)}(k)$ , for spanwise Fourier modes,  $k$ . The eigenvalues for each  $k$  is summed over POD mode numbers,  $n$ .

present, and there to be no overlap region at all. These results are certainly consistent with their suggestions.

### B. Eigenvalue Distribution over the POD and Spanwise Fourier Modes

The eigenspectra of the POD modes can be integrated over frequency to investigate the kinetic energy distribution over the spanwise Fourier modes as shown in figure 3. In this case, the eigenvalues are presented in their normalized form using (13):

$$\xi^{(n)}(k) = \frac{\int_{-\infty}^{\infty} \lambda^{(n)}(k, f) df}{\sum_{k=1}^M \sum_{n=1}^N \int_{-\infty}^{\infty} \lambda^{(n)}(k, f) df} \quad (13)$$

where  $M$  and  $N$  are the maximum number of Fourier modes in the spanwise direction and POD modes respectively. Each bar in figure 3 denotes the turbulence kinetic energy for a particular spanwise Fourier mode, which also means that the bars show the eigenvalues summed over POD

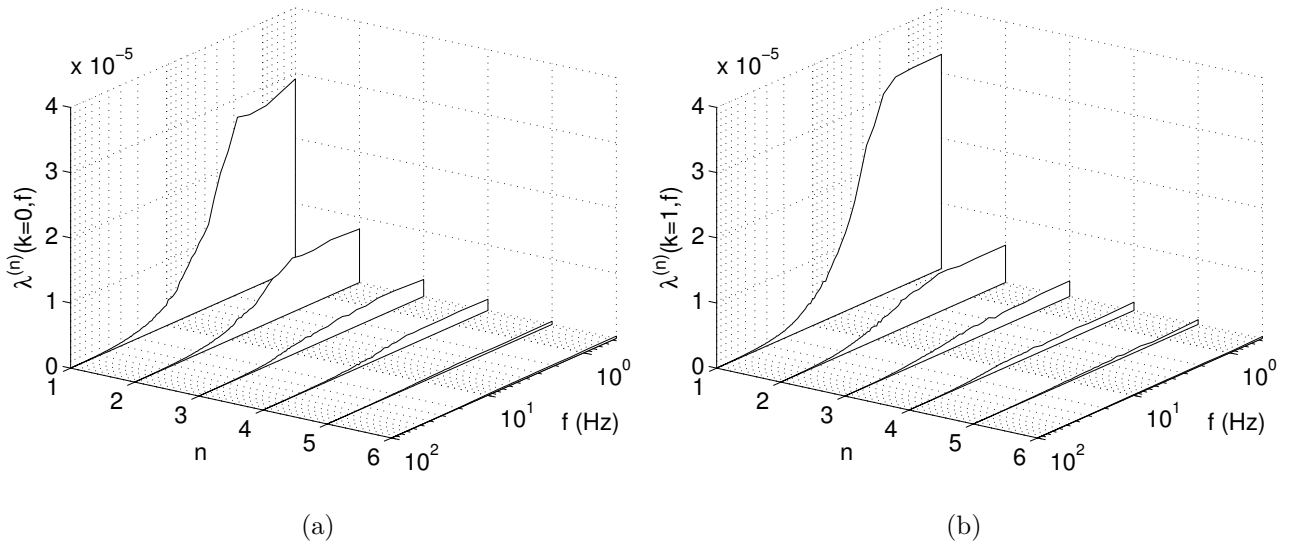


FIG. 4. Eigenspectra,  $\lambda^{(n)}(k, f)$ , of the first 2 spanwise Fourier modes ( $k = 0$  and  $3$ ) for different POD modes,  $k$ , and frequencies,  $f$ , at  $\text{Re}_\theta = 19\ 100$ .

modes for a given  $k$ . Only first 13 spanwise modes ( $k = 0, 1, \dots, 12$ ) are shown to identify the relative contribution of the most important spanwise modes clearly. It can be easily seen that spanwise Fourier modes higher than 3 have small, and therefore insignificant, contribution to the total energy. Note that there are 71 spanwise Fourier modes; symmetric pairs of 35 modes plus the zeroth Fourier mode. Therefore, the first spanwise Fourier mode ( $k = 1$ ) and the last spanwise Fourier mode ( $k = 71$ ) are identical and so forth. In figure 3, we do not show the symmetric part.

As mentioned earlier, it is difficult to see any Reynolds number dependency in our results presented so far. Integration over frequency smooths out some of the difference which we might have expected to see. Therefore the distribution of eigenvalues for these two cases are very close to each other with no apparent dependence on the Reynolds number. Common features of these figures can be listed as: (i) Most of the energy is found at spanwise Fourier mode-0 and mode-1, (ii) Spanwise Fourier mode-1 is slightly larger than spanwise Fourier mode-0 at both Reynolds numbers.

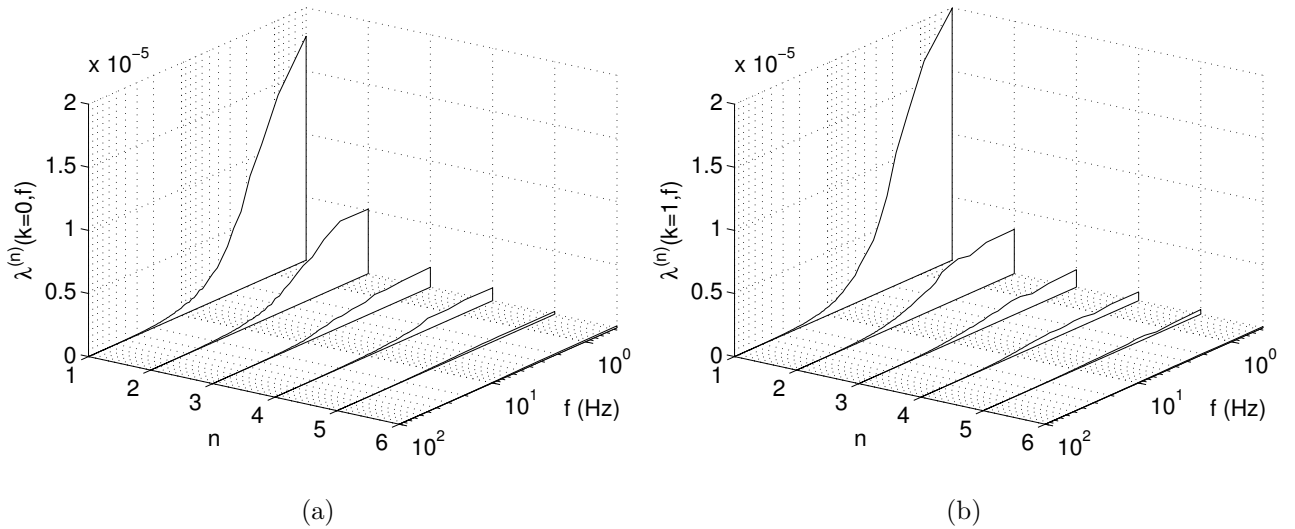


FIG. 5. Eigenspectra,  $\lambda^{(n)}(k, f)$ , of the first 2 spanwise Fourier modes ( $k=0$  and  $1$ ) for different POD modes,  $k$ , and frequencies,  $f$ , at  $\text{Re}_\theta = 9800$ .

### C. Eigenspectra over the Spanwise Fourier Modes, $k$ , and Frequency, $f$

The POD integral equation is solved for each spanwise Fourier mode ( $k$ ) and frequency ( $f$ ) as in equation (6). The eigenvalues (or eigenspectra in this case) and eigenfunctions become functions of both  $k$  and  $f$ . To illustrate the distribution of eigenvalues over the spanwise Fourier modes and frequencies, and to highlight some of the frequency dependency of eigenspectra at different Reynolds numbers, we present  $\lambda^{(n)}(k, f)$  in figures 4 and 5 for the  $\text{Re}_\theta$  of 19 100 and 9800 respectively. In order to focus on the most energetic modes, the first two spanwise Fourier modes ( $k = 0, 1$ ) are displayed. The amount of energy carried by the spanwise Fourier modes which are higher than  $k = 1$  is very small compared to the first two spanwise Fourier modes, and not presented here. The highest POD mode and frequency considered in these figures are 6 and 100 Hz, respectively. This is because the contributions of higher modes and frequencies are not significant in terms of magnitude.

Figures 4 and 5 demonstrate that all eigenspectra peak at the near zero frequency. This phenomenon is more pronounced for the first POD modes at both Reynolds numbers. We observe a faster decay of energy for the low Reynolds number case. General features of the eigenspectra are very similar for both Reynolds numbers. One should note that the eigenspectra shown in

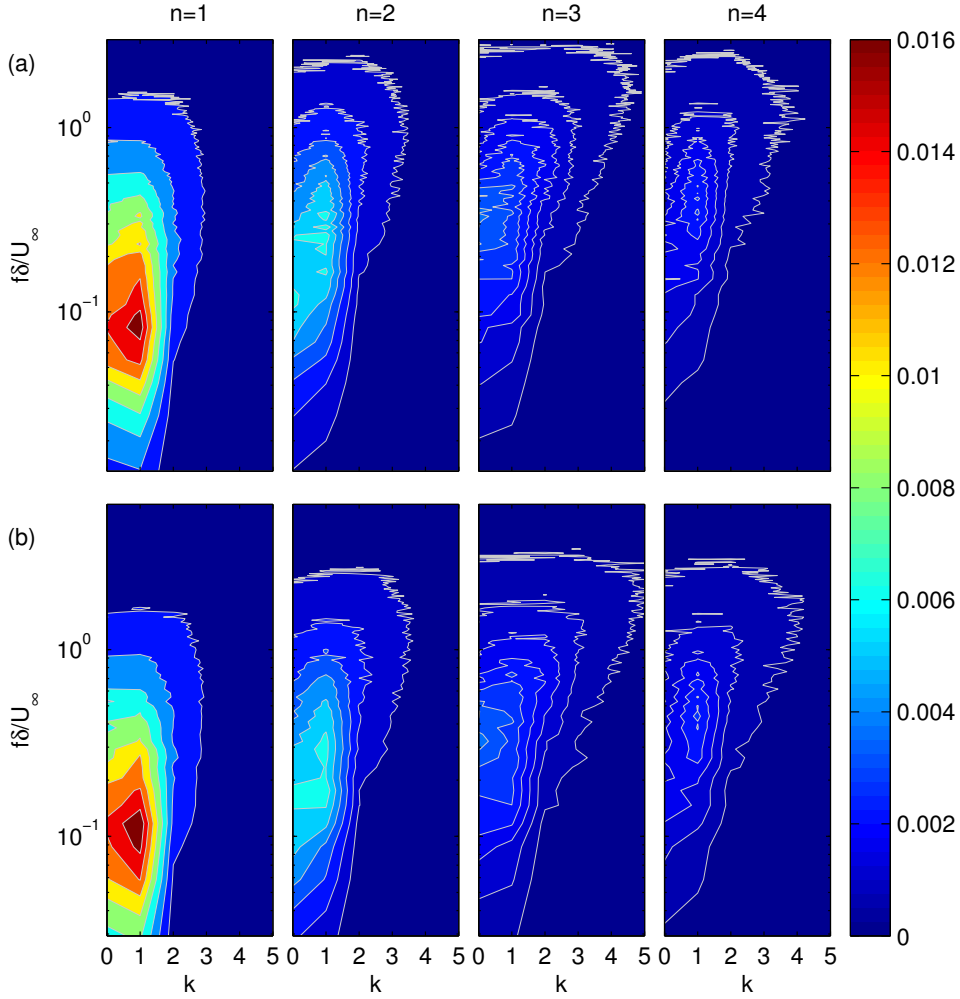


FIG. 6. Pre-multiplied eigenspectra,  $f\Lambda^{(n)}(k,f)$ . (a)  $Re_\theta = 19100$ ; (b)  $Re_\theta = 9800$ . Eigenvalues are normalized by turbulence kinetic energy due to streamwise fluctuations within the domain.

figures 4 and 5 are not normalized by the total turbulence kinetic energy within the domain. Therefore, eigenvalues from the high Reynolds number measurement are approximately double those from the low Reynolds number measurement. This is expected, because the increase in Reynolds numbers was achieved by increasing the tunnel speed, which caused an almost directly proportional increase in rms velocities.

Figure 6 displays the pre-multiplied eigenspectra, normalized as described in equation (14), for the most energy carrying eigenfunctions:

$$\Lambda^{(n)}(k, f) = \frac{\lambda^{(n)}(k, f)}{\sum_{n=1}^N \sum_{k=1}^M \int_{-\infty}^{\infty} \lambda^{(n)}(k, f) df} \quad (14)$$

The frequency axes in figure 6 are normalized using the boundary layer thickness and the freestream velocity. The normalized frequency ( $f\delta/U_\infty$ ) extends from 0.03 to 6 in low Reynolds number case, and from 0.013 to 3 for high Reynolds number case. (Note that the corresponding upper limits in dimensional frequencies are approximately 50 Hz and 100 Hz for low and high Reynolds numbers, respectively.) Pre-multiplied eigenspectra,  $f\Lambda^{(n)}(k, f)$ , at both Reynolds number show similar features. The peaks of the pre-multiplied eigenspectra in both cases are found to be around  $f\delta/U_\infty$  of 0.1. The extent of the energy carrying modes in non-dimensional frequency axes is also similar to each other. Likewise, large eigenspectral values representing the modes carrying large amount of turbulence kinetic energy are bounded by the spanwise Fourier mode number 4.

Figure 7 compares the first two POD modes of both Reynolds numbers shown in figure 6. Contour lines of the pre-multiplied eigenspectra at both Reynolds numbers agree very well when the outer scaling parameters,  $\delta$  and  $U_\infty$ , are used to normalize the frequency axes. (Note that we follow GC97<sup>39</sup> in our choice of outer variable for the boundary layer.) On the other hand, the agreement is completely lost when the inner scaling parameters are used for normalization, see figure 8.

These results essentially agrees with previous finding of Liu et al.<sup>23</sup> even though the flow in their case was turbulent channel flow. Liu et al.<sup>23</sup> showed that the Reynolds number similarity of the eigenvalues of fully developed channel flow exists when the outer scaling parameters are used in the outer layer. They further stated that “in the region outside the wall layer and in the range of sequences where the wavelength is large compared to the wall layer viscous length scale, both the eigenfunctions and the spectrum of eigenvalues when scaled by outer layer variables are independent of the Reynolds number for sufficiently large Reynolds number”. In addition, they also documented some similarity between the behavior of eigenvalues obtained from channel flow measurements and boundary layer measurements. (Note that outer scaling for the pipe or channel flows uses  $u_\tau$  and channel height or pipe radius, respectively, cf. Wosnik et al<sup>40</sup>.) One difference which should be mentioned here is the fact that our analysis is based

on an extended domain, from wall to freestream, whereas Liu et al.<sup>23</sup> only focused on the outer layer. The much lower Reynolds number of their experiments made such a partition of their results necessary, since the outer flow was not of great enough extent to dominate as it does in ours.

In order to understand why eigenspectra scale better with the outer scaling parameter, it is useful to revisit how POD works and decomposes the domain, which is approximately  $\delta \times \delta$  on a plane perpendicular to the streamwise direction in our case. As a matter of fact, POD finds modes of turbulence in the inhomogeneous coordinate direction with finite total energy, and then sorts them according to their energy content. Figures 7 and 8 suggest that POD modes carrying large amount of turbulence kinetic energy are physically large in the wall-normal direction as well. This means that they have great portion of their physical size in the outer part of the boundary layer. Blackwelder and Kovasznay<sup>41</sup> showed that contribution of the large scale eddies to turbulence kinetic energy was about 50% and that to the Reynolds shear stress was approximately 80% in the outer layer. Similar findings are also documented by Guala et al.<sup>42</sup> for turbulent pipe flow. In a more recent study, Tutkun et al.<sup>30</sup> carried out extensive two-point correlation analysis and showed the strong correlation between near-wall and outer layer. The Reynolds number similarity of the lower POD modes once scaled by the outer flow parameters can therefore be attributed to the large and very large eddies connecting the near-wall region and outer layer<sup>30,43</sup>.

#### D. Pre-multiplied Spectra

Large- and very large scale motions (LSM and VLSM) of wall-bounded turbulent flow have recently received considerable attention by researchers<sup>27,30,42–46</sup>. The main interest is the correlation between the size of scales and their contribution to the turbulence kinetic energy and Reynolds shear stress, particularly in the outer layer. Pre-multiplied one-dimensional wavenumber spectra are often studied to learn about the length scales associated with large eddies and wall-normal positions where these large scale motions are observed. It is therefore useful to compare the pre-multiplied normalized eigenspectra (figure 6) with the pre-multiplied velocity spectra (figure 9). Note that figure 9 is reproduced from the pre-multiplied one-dimensional wave number spectra of the streamwise velocity fluctuations presented in figure 2 of Tutkun et

al.<sup>30</sup>. The wave-number spectra were originally obtained from the frequency spectra using the Taylor’s frozen field hypothesis.

Figure 9 presents pre-multiplied velocity spectra,  $fS_{11}(f)/u_7^2$ . Scaling of the frequency axis of figure 9 is performed using outer scaling parameters which are also used in the eigenspectra shown in figure 6. One should note that these parameters may not be the most appropriate ones for the one-dimensional velocity spectra, however it is difficult to assign a true convection velocity to eigenfunctions. Converting the frequency axes into a wavenumber axes, or wavelength, by means of Taylor’s frozen field hypothesis is not easy in the absence of an accurately defined convective velocity. Therefore, the data are presented in frequency domain.

Pre-multiplied velocity spectra in figure 9 show two regions where the turbulence kinetic energy peaks: one near the wall, also corresponding to near-wall peak of turbulence kinetic energy, and another one in the inertial layer. The near-wall peaks are at  $y^+$  of  $\sim 10$  and  $\sim 15$  for high and low Reynolds numbers respectively. The secondary peaks are observed between  $y^+$  of 220 and 580 at  $Re_\theta$  of 19 100 (corresponding to  $0.03\delta$  and  $0.08\delta$ ) and  $y^+$  of 150 and 340 at  $Re_\theta$  of 9800 (corresponding to  $0.04\delta$  and  $0.09\delta$ ). Figure 6, by contrast, shows only one distinct peak in the pre-multiplied eigenspectra. The peak of the eigenspectra appears approximately at the same frequency where the secondary peak of the pre-multiplied velocity spectra appears.

The frequency of the outer peak of the pre-multiplied velocity spectra coincides with the frequency of the peak of the eigenspectra. The other combinations such as using inner scaling for pre-multiplied velocity spectra and outer scaling for pre-multiplied eigenspectra, or vice versa, do not make the near-wall peak of the pre-multiplied velocity spectra overlap with the peak of pre-multiplied eigenspectra. Even though the peaks of the pre-multiplied eigenspectra are approximately at  $f\delta/U_\infty$  of 0.1 at both Reynolds numbers, normalized pre-multiplied velocity spectra show the peaks between  $f\delta/U_\infty$  of 1.5 and 4 at the high Reynolds number and 0.9 and 3 at the low Reynolds number. The wavelength of the scales of motion in the streamwise direction can be approximated by dividing the corresponding convection velocity by the frequency of the scale ( $\lambda_1 = U_c/f$ ; where  $U_c$  denotes the convection velocity). Therefore, it seems that it is impossible to have similar wavelengths for the peak of pre-multiplied eigenspectra and the near-wall peak of pre-multiplied velocity spectra, unless the convection velocity of the large scales captured by the POD eigenmodes is 30 times larger than the local mean velocities occurring

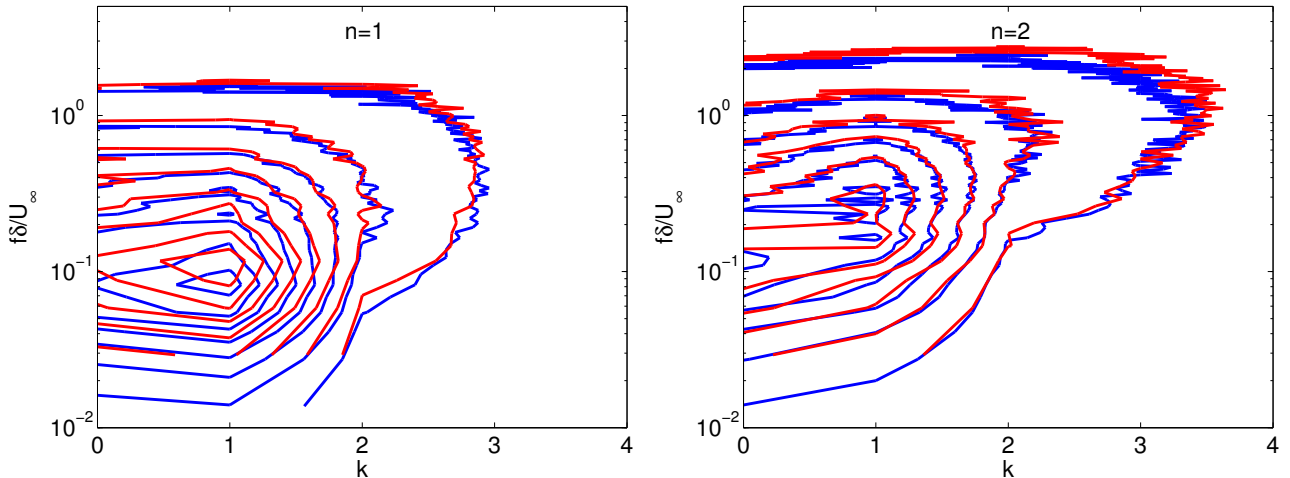


FIG. 7. Pre-multiplied normalized eigenspectra,  $f\Lambda^{(n)}(k,f)$  for the first 2 POD modes,  $n=1$  and 2 as a function of frequency, normalized by boundary layer thickness ( $\delta$ ) and freestream velocity ( $U_\infty$ ), and Fourier mode,  $k$ . Solid black and dashed gray lines represent the high Reynolds number case and low Reynolds number case respectively. For  $n=1$ , the contour values: (0.002 (outermost), 0.004, 0.006, 0.008, 0.010, 0.012, 0.014, 0.016 (innermost)). For  $n=2$ , the contour values: (0.001 (outermost), 0.002, 0.003, 0.004, 0.05, 0.006 (innermost))

near the wall at  $y^+$  of 10-20. This kind of large convection velocity indeed exceeds the freestream velocity. Therefore, it can be concluded that the single peak seen in the eigenspectra and the near-wall peak of the velocity spectra have different physical origins. Careful examination of the pre-multiplied eigenspectra in comparison with the pre-multiplied velocity spectra suggests that underlying reasoning for the peak of the eigenspectra and the secondary peak of the velocity spectra is most likely the same.

The secondary peak of the pre-multiplied velocity spectra inside the inertial (or log) layer has been clearly identified and discussed by many researchers<sup>27,30,43,46,47</sup>. The pre-multiplied velocity spectra are essentially based on single-point statistics. Therefore, it actually does not take the lateral and transverse extent of the scales into account, and puts more weight on scales which are elongated in the streamwise direction. On the other hand, the POD, because of its kernel which is the two-point correlations, considers the lateral and transverse extent of the scales within the domain. In light of these, the results presented so far suggest that the scales

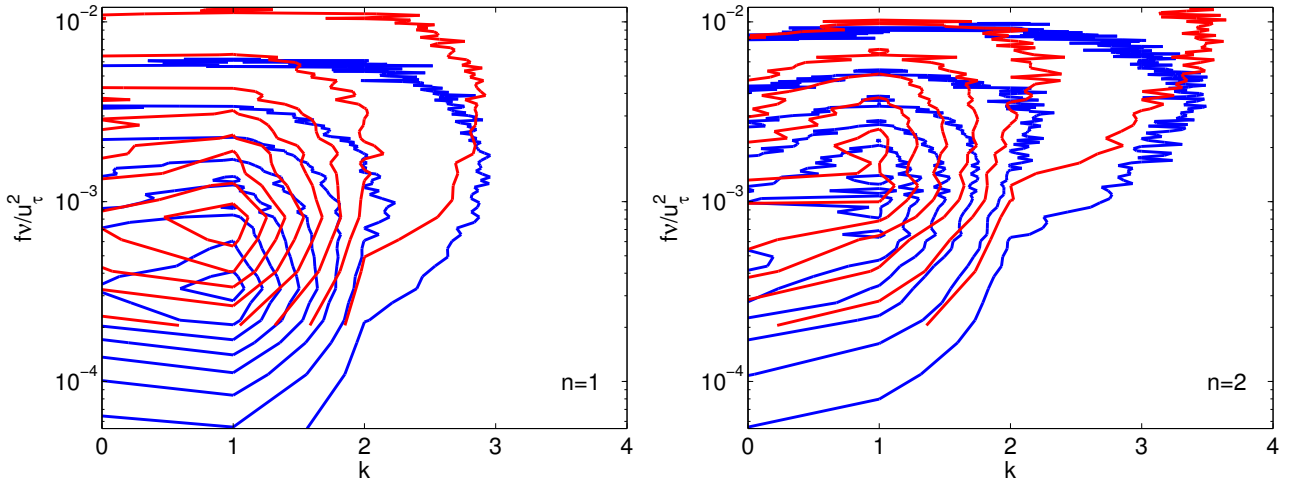


FIG. 8. Pre-multiplied normalized eigenspectra,  $f\Lambda^{(n)}(k,f)$  for the first 2 POD modes,  $n=1$  and 2 as a function of frequency, normalized by viscous length ( $\nu/u_\tau$ ) and friction velocity ( $u_\tau$ ), and Fourier mode,  $k$ . Solid black and dashed gray lines represent the high Reynolds number case and low Reynolds number case respectively. For  $n=1$ , the contour values: (0.002 (outermost), 0.004, 0.006, 0.008, 0.010, 0.012, 0.014, 0.016 (innermost)). For  $n=2$ , the contour values: (0.001 (outermost), 0.002, 0.003, 0.004, 0.05, 0.006 (innermost))

creating the secondary peak of pre-multiplied velocity spectra are large and coherent in both wall-normal and spanwise directions. These scales also contain more energy when compared to the scales responsible for the near-wall peak. It should however be noted that this can only be observed at large enough Reynolds numbers which ensure a separation of scales. A low Reynolds number leads to absence of a clear inertial layer, and large scale energetic motions of the outer layer will be strongly felt near the wall. This shifts the location of the single peak of pre-multiplied eigenspectra toward the near-wall peak of pre-multiplied velocity spectra.

Figure 10 displays the pre-multiplied spectra with respect to wall-normal position and frequency axes scaled with the wall-normal position ( $y$ ) and the friction velocity ( $u_\tau$ ). In this case both inner and outer peaks of the pre-multiplied velocity spectra are at  $fy/u_\tau \sim 0.1$ . As a matter of fact, one cannot use ratio of  $y/u_\tau$  to normalize the frequency axes of eigenspectra because each eigenvalue is defined across the domain. This scaling presumes that the size of the eddies is proportional to the location of the eddies with respect to the wall, i.e., the basis

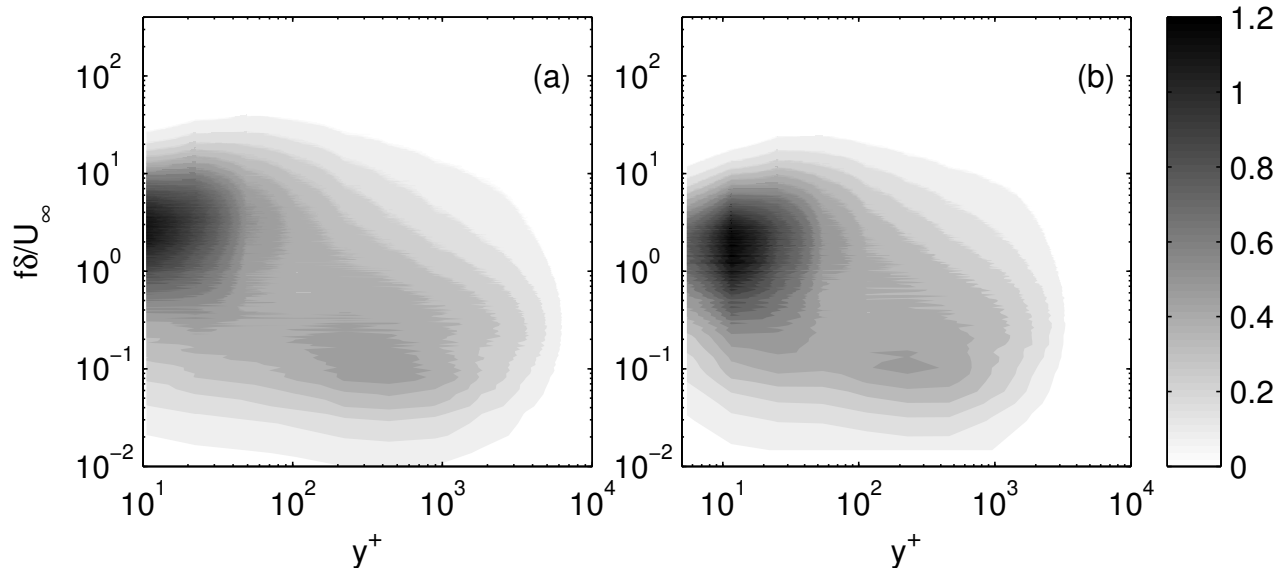


FIG. 9. Pre-multiplied spectra  $f\delta_{11}(f)/u_\tau^2$  as a function of frequency,  $f$ , normalized by boundary layer thickness,  $\delta$ , and freestream velocity,  $U_\infty$ : (a)  $Re_\theta$  of 19 800, (b)  $Re_\theta$  of 9800.

of the Townsend's attached eddy hypothesis<sup>48</sup>. This explains why we observe a single peak in the pre-multiplied eigenspectra at the frequencies where we also observe the secondary peak of the pre-multiplied velocity spectra. If the turbulent boundary layer is a hierarchy of eddies at different size from wall to the freestream, e.g., figure 15 of Adrian<sup>47</sup>, the near-wall region will have the contributions of both small, large and very large scales of motion. Therefore, the peak of turbulence kinetic energy due to streamwise velocity fluctuations around  $y^+$  of 10-15 has contributions from all of these scales. Most of the physical size of the large and very large eddies, however, are actually in the outer layer. This was exactly the point of GC97<sup>39</sup> who inferred the outer effect on the inner flow from the two-point correlations documented by Blackwelder and Kaplan<sup>49</sup>. Since the two-point information is built into the kernel of the POD, it links between the different layers of the turbulent boundary layer.

### E. Velocity Profiles

The reconstructed velocity field, formulated in section IV B, provides further support to these ideas. Using the POD eigenmodes, it is possible to reconstruct the global velocity field.

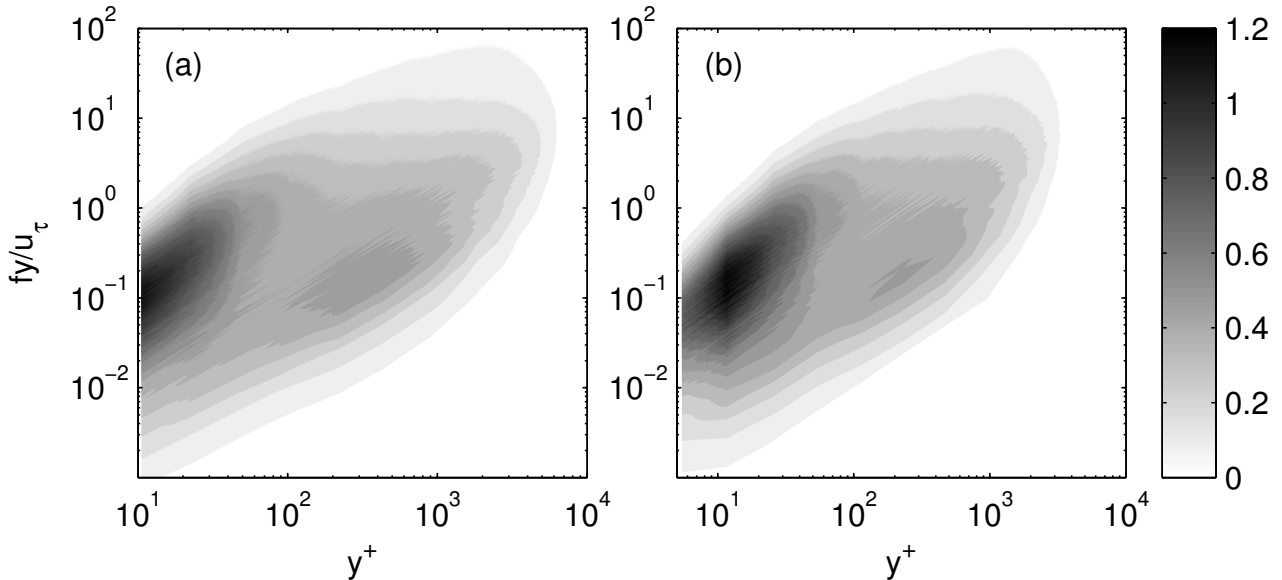


FIG. 10. Pre-multiplied spectra  $fS_{11}(f)/u_\tau^2$  as a function of frequency,  $f$ , normalized by wall-normal position,  $y$ , and friction velocity,  $u_\tau$ : (a)  $Re_\theta$  of 19 800, (b)  $Re_\theta$  of 9800.

The velocity field can also be reconstructed using selected modes, in particular the most important ones. This is achieved by setting the random coefficients of the excluded modes to zero while reconstructing the velocity field. Equation (11) produces the instantaneously fluctuating velocity field, since the back-projection is performed over the fluctuating velocity field itself. Then, turbulence statistics based on the reconstructed velocity signals can be studied.

Figure 11 shows the reconstructed rms velocity profiles across the turbulent boundary layer at both Reynolds numbers tested in this study. The solid lines in these figures present the measurements of Carlier and Stanislas<sup>33</sup>, which were also measured using the same wind tunnel at approximately the same Reynolds numbers. Since the main interest here is to look at the behavior of energetic fluctuations in a statistical sense, first a reconstruction of global velocity field has been performed using only the most energy carrying modes. The profiles created by the energetic large scale modes are denoted by the circles. The modes included in reconstruction shown by the circles are the first 4 POD modes, spanwise Fourier modes 0, 1, 2, 3 and their symmetric pairs, and frequencies up to 100 Hz in the high Reynolds number case, and up to 50 Hz in the low Reynolds number case.

Reconstruction in this way recovers 62% of the turbulence kinetic energy in high Reynolds number case, but only 0.024% of total number of modes which can be extracted from the domain. This *energetic reconstruction* enables a tremendous reduction when total number of degrees of freedom is concerned. The profiles formed by triangles denote the rms of streamwise velocity fluctuations obtained from the *non-energetic reconstruction* of the remaining 99.976% of the total number of modes; i.e. those that were discarded from the initial reconstruction. In the same figure, we also included the profile of the full reconstruction using every mode extracted from the field. The full reconstruction is presented by the squares and matches the data of Carlier and Stanislas<sup>33</sup> perfectly. (One should note that if one adds rms profile obtained from partial reconstructions using both energetic and non-energetic, e.g., circles plus triangles, the summation is always larger than the rms obtained from the full reconstruction. The correct way is to add reconstructed instantaneous velocity signals both from the energetic and non-energetic reconstructions first, and then to compute the statistics afterward.)

The rms profiles produced by the energetic modes representing the large scales and those by the scales with small to negligible amount of energy have some distinct features. For the  $Re_\theta = 19100$  case, reconstruction of the energetic modes reveal the following: (i) the rms profile from  $y^+$  of 20 to 50 shows an exponential decay, (ii) from  $y^+$  of 50 to top of the inertial layer, the rms of the velocity fluctuations is constant, (iii) the constant layer within the inertial layer is followed by another exponential decay (with a different slope this time). On the other hand, the reconstruction using the less energetic modes at this high Reynolds number shows: (i) an exponential decay of turbulence kinetic energy after the peak of total turbulence kinetic energy until the top of the logarithmic layer, i.e.,  $20 \lesssim y^+ \lesssim 450$ ; and (ii) a constant layer of energy after the inertial layer, for  $y^+ \gtrsim 900$ . In addition, the slopes of the decay of turbulence kinetic energy due to energetic part below  $y^+$  of 50 and that due to non-energetic part between  $y^+$  of 20 to top of the logarithmic layer are approximately the same.

A similar analysis for the  $Re_\theta = 9800$  measurement clearly shows the low Reynolds number effects. Since the physical distances between the wall and the probes of the hot-wire rake are fixed, the first row of hot-wire probes for the low Reynolds number case measured closer to the wall in wall-units. Therefore, we observe the effect of viscosity and the boundary conditions imposed by the wall when  $y^+ \lesssim 15$ . This effect is indeed present in both energetic and non-

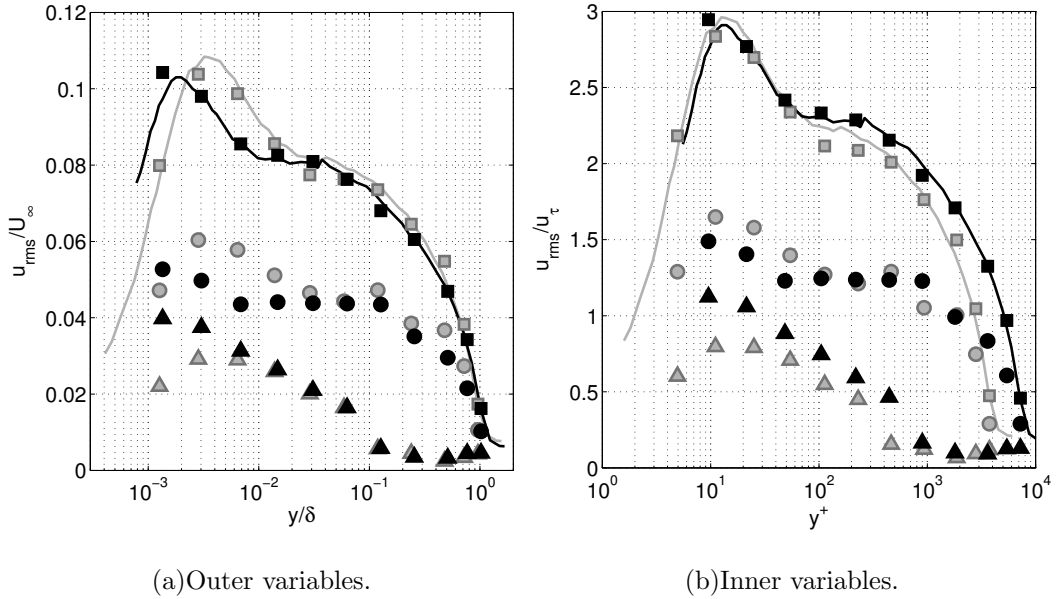


FIG. 11. Comparison of rms velocity profiles of velocity obtained from full and partial reconstructions. Black color presents the high Reynolds number case ( $Re_{\theta} = 19100$ ), and gray color presents the low Reynolds number case ( $Re_{\theta} = 9800$ ). Lines present the data of  $f^{33}$ ; Circles denote rms profile of reconstructed global velocity field using first 4 POD modes ( $n=1, 2, 3, 4$ ), first 4 spanwise Fourier modes and their symmetric pairs ( $k=0, \pm 1, \pm 2, \pm 3$ ), and frequencies up to 100 Hz at  $Re_{\theta} = 19100$  case and 50 Hz at  $Re_{\theta} = 9800$  case. Triangles present the profiles obtained from the reconstruction based on all of the modes and frequencies except the ones presented by the circles. Squares represent the full reconstruction using every mode and frequency.

energetic reconstructions. The rms profile based on the energetic reconstruction at  $Re_{\theta} = 9800$  shows: (i) an exponential decay of turbulence kinetic energy between  $y^+$  of 25 and 114, (ii) a constant layer between  $y^+$  of 114 and 465, (iii) an exponential decay between  $y^+$  of 465 and 2800. The non-energetic construction in this case shows: (i) the exponential decay of turbulence kinetic energy at  $25 \lesssim y^+ \lesssim 230$  and (ii) a constant layer in the outer layer where  $y^+ \gtrsim 900$ .

In order to facilitate a better comparison between the results obtained at two different Reynolds numbers, the effect of utilizing different scaling parameters, both inner and outer, are also studied. Figures 11(a) and 11(b) present outer scaled profiles and inner scaled profiles, respectively. As known widely, the inner scaling produces a better collapse in the near wall

region, whereas the outer scaling (of GC97<sup>39</sup>) results in a better agreement in the outer part of the boundary layer. This can be easily seen in the measurement of Carlier and Stanislas<sup>33</sup>. Statistics on the partial reconstructions shown in figure 11, on the other hand, reveal a different picture as detailed below.

We observe an overlap of the profiles of the energetic reconstructions at both Reynolds number in inertial layer whose extent is smaller for the low Reynolds number case due to well-known low Reynolds number effects. The profiles obtained from the energetic reconstruction do not produce an overlap in the near wall region at all. This can be attributed to the size and energy of the scales used in the reconstruction and their dependence on the boundary conditions. On the other hand, the rms outputs of these two different reconstructions have approximately the same slopes below the inertial layer. This means that the way the wall and the energetic/non-energetic parts of the turbulence interact is quite similar.

As a matter of the fact, one sees very good collapse of the velocity profiles near the wall when two profiles obtained by the non-energetic reconstruction are compared using the inner scaling parameters, e.g., see figure 11(b). This is perhaps due to the fact that the small scale fluctuations, which are not energetic in this framework, are more affected by the wall. However, figure 11(b) reveals that the inner scaling does not actually do a good job from wall to  $y^+ \sim 900$ . The only place where the inner scaling indicated a reasonable agreement when both non-energetic reconstructions are combined is the outer part of the boundary layer, i.e.,  $y^+ \gtrsim 900$ . This is somewhat surprising because scaling based on inner (or wall) parameters works very well on the non-energetic part in the region where the wall is thought to be not important at all. One may, then, conclude that the wall scaling parameters are actually not the most relevant in this case. This especially makes sense if the boundary layer is indeed driven and controlled by the energetic large scale structures of the outer layer, which is actually suggested by the pre-multiplied spectra shown earlier in present paper. One should also note that outer scaling performs much better for non-energetic reconstruction when  $y^+ \gtrsim 900$ .

Figure 11(a) shows the outer scaled profiles. The energetic reconstructions in this case collapse very well in the inertial layer (the flat region), which is one of the common features observed in both inner and outer scaling. The outer scaling does not yield a collapse of profiles from wall to beginning of the constant layer, which corresponds to beginning of the inertial layer.

The energetic reconstruction scaled using outer parameters agrees very well in the outer layer. On the other hand, the outer scaling produces very good collapse of the non-energetic turbulence from the top of the boundary layer down to the wall-normal location where the viscosity takes over and dominates everything. This indicates that the small scale, non-energetic, turbulence away from the wall does not depend on the presence of the wall.

The results presented in preceding pages revealed that the large scale energetic turbulence inside the boundary layer scales with the outer layer parameters. This means that the small scale, non-energetic turbulence is controlled by the large scale energetic turbulence. Otherwise, we would not observe a good collapse of the small scale turbulence when the profiles are scaled with the outer parameters. This essentially agrees with a recent paper by Mathis et al<sup>50</sup> where they documented modulation of small scales by the large-scales of outer layer in a turbulent boundary layer study and showed the strong interaction between large scale log-layer motions and small scale near-wall motions.

Another important finding in figure 11 is the behavior of the layer of constant rms of velocity fluctuations at two different Reynolds numbers. As the Reynolds number increases, the constant layer widens in both directions and propagates toward the wall. This is perhaps due to the fact that the viscosity dominated part of the turbulent boundary layer gets thinner as the Reynolds number increases. Therefore, the large and energy carrying scales which populate significantly the inertial and outer layers find more space to occupy without feeling the presence of solid wall. For the low Reynolds number case, the scale separation between the large and small scale turbulence is very small. This is evidenced by the very short constant layer of rms profile shown in figure 11. These findings clearly prove the early statement of GC97<sup>39</sup> which essentially suggested that a proper inertial layer begins to emerge at  $Re_\theta \approx 10\,000$ .

## VI. SUMMARY AND CONCLUSIONS

In this paper, experimental utilization of the proper orthogonal decomposition for the high Reynolds number flat plate turbulent boundary layer is studied. The data was obtained in the large LML wind tunnel, The boundary layer thickness was approximately 30 cm in the end of 21.6 m long test section. The streamwise component of the turbulent boundary layer velocity field was measured using a hot-wire rake of 143 probes. The array of probes enabled

simultaneous sampling and therefore computing the cross-spectral tensor which formed the kernel of the Lumley integral equation.

The normalized eigenvalue distribution shows that the first POD mode integrated over frequency and azimuthal mode number has more than 40% of the turbulence kinetic energy, while the second one has about 20% of the total turbulence kinetic energy. It is possible to recover about 90% of the kinetic energy only using the first four POD modes. Similar figures are obtained at both Reynolds number with no significant indication of Reynolds number dependence.

The eigenspectra always peak near zero frequency and most of the large scale features are found below 100 Hz and 50 Hz for the high and low Reynolds number cases studied here respectively. This could be the effect of aliasing from the missing dimension as suggested by George<sup>2</sup>. The results indicate that it might be possible to scale the eigenspectra especially in the inertial range of turbulence similar to the similarity of the eigenfunctions and eigenspectra within the outer layer of turbulent wall flow. The kinetic energy distribution is maximum at spanwise Fourier mode-1, while there is a slight difference between spanwise Fourier mode-0 and-1. The normalized eigenvalue distribution obtained from two different Reynolds numbers have almost the same distribution and features.

The pre-multiplied eigenspectra are produced in a similar fashion as the pre-multiplied velocity spectra. Instead of wave-number spectra, frequency domain spectra were used because of difficulty in assigning a true convective velocity. The pre-multiplied eigenspectra have only one peak whereas the pre-multiplied velocity spectra have two peaks; one in the near-wall region and another one in the log-layer. The comparison between the pre-multiplied velocity spectra and the pre-multiplied eigenspectra shows that frequency of the peak of pre-multiplied eigenspectra coincides with frequency of the secondary peak observed in the pre-multiplied velocity spectra. This means that the large scale modes of turbulent boundary layer are indeed connected to the physical mechanisms causing the secondary peak of the pre-multiplied velocity spectrum. In support of this, tests of inner and outer scaling of pre-multiplied eigenspectra at both Reynolds numbers suggested the outer scaling parameters outperform the inner scaling parameters. One should always note that the near-wall peak in turbulence kinetic energy is confined to a very small area, only a few percent of  $\delta$ , as we consider the entire turbulent boundary layer. In fact, 90% of the boundary layer is outer flow. Even though the magnitude of local turbulence

kinetic energy is large near the wall, its net contribution to the total turbulence kinetic energy is small. It is therefore not surprising to see only one peak in pre-multiplied eigenspectra away from the near-wall region.

Reconstructed velocities were studied to see the effect of energetic and non-energetic modes of the POD on the turbulence statistics. At both Reynolds numbers, the rms profiles based on *energetic reconstruction* (with modes carrying significant amount of energy) and that based on *non-energetic reconstruction* (with modes carrying very small amount energy, and essentially the modes which are not considered energetic) indicate three distinct behaviors of the fluctuating velocities across the boundary layer. The higher Reynolds number case produces better defined layers due to absence of low Reynolds number and viscosity effects. The reconstructed rms based only on the energetic part of the modes decays exponentially between the log-layer and the wall, stays approximately constant through the log-layer, then decays exponentially after the log-layer. On the other hand, the non-energetic reconstruction shows that  $u_{\text{rms}}$  decays exponentially from wall to the top of the log-layer and stays flat at its minimum once the log-layer is over. Similar pictures are also seen in lower Reynolds number test, but this time the effect of viscosity and Reynolds number effects are observed. This is because the probe locations are fixed in both cases, while the wall unit is doubled in the low Reynolds number case. The outer scaling seems performs much better for both energetic and non-energetic reconstructed statistics which suggests that small scale motions right outside the inner sublayer are strongly influenced by the large scale outer layer motions.

These findings supports earlier findings of Tutkun et al<sup>30</sup>, in which authors showed the strong connection between the near-wall region and outer layer by studying the two-point correlations of the same data. Amplitude modulation of small-scale motions near the wall by the large scale motions of outer layer has previously been documented for both turbulent boundary layer flow and turbulent channel flow<sup>50</sup>. The statistics of reconstructed turbulence based on our POD results indicate that large energy carrying POD modes strongly influence the small-scale, non-energetic, fluctuations, not only in near-wall region but also throughout the boundary layer.

## Appendix A: POD Analysis Procedure and Numerical Implementation

The POD integral equation given by Eq. (6) can be solved numerically by approximating the integral using the trapezoidal rule:

$$\int_{y'} f(y') dy' \approx \sum_{i=1}^N f_i \Delta y'_i \quad (\text{A1})$$

where  $f_i$  and  $\Delta y'_i$  represent the values of the function  $f$  at the grid points (or measurement points in this case) and value of the integrand around these grid points respectively. Justification of using the trapezoidal rule in computing the POD integral equation is detailed by Moin and Moser<sup>16</sup>. The numerically discretized form of the POD integral equation, Eq. (6), results in an eigenvalue problem, which can be written as follows:

$$\mathbf{A}\phi^{(n)} = \lambda^{(n)}\phi^{(n)} \quad (\text{A2})$$

Solution to the eigenvalue problem given by Eq. (A2) is easy to obtain using a standard numerical eigenvalue solver if the kernel,  $\mathbf{A}$ , is Hermitian symmetric. Because of the logarithmic stretching of the probes along the wall-normal direction, the  $\mathbf{A}$  in this experiment is not Hermitian symmetric as shown below:

$$\mathbf{A} = \begin{bmatrix} S_{1,1}(y_1, y'_1; k; f) & S_{1,1}(y_1, y'_2; k; f) & \cdots & S_{1,1}(y_1, y'_N; k; f) \\ S_{1,1}(y_2, y'_1; k; f) & S_{1,1}(y_2, y'_2; k; f) & \cdots & S_{1,1}(y_2, y'_N; k; f) \\ \vdots & \vdots & \ddots & \vdots \\ S_{1,1}(y_N, y'_1; k; f) & S_{1,1}(y_N, y'_2; k; f) & \cdots & S_{1,1}(y_N, y'_N; k; f) \end{bmatrix} \begin{bmatrix} \Delta y'_1 & 0 & 0 & 0 \\ 0 & \Delta y'_2 & 0 & 0 \\ \vdots & \vdots & \ddots & \vdots \\ 0 & 0 & 0 & \Delta y'_N \end{bmatrix} \quad (\text{A3})$$

where the first matrix is the two-point cross-spectral tensor and the second matrix is the diagonal matrix with the integrands. The remedy to make the kernel Hermitian symmetric is to rearrange Eq. (A2) and multiply both sides of it with the diagonal matrix of square-roots of the integrands:

$$\underbrace{\mathbf{wS}}_{\mathbf{H}} \underbrace{\mathbf{w}\phi^{(n)}}_{\psi^{(n)}} = \lambda^{(n)} \underbrace{\mathbf{w}\phi^{(n)}}_{\psi^{(n)}} \Rightarrow \mathbf{H}\psi^{(n)} = \lambda^{(n)}\psi^{(n)} \quad (\text{A4})$$

where  $\mathbf{w}$ ,  $\mathbf{S}$  and  $\phi^{(n)}$  are:

$$\mathbf{w} = \begin{bmatrix} \sqrt{\Delta y'_1} & 0 & 0 & 0 \\ 0 & \sqrt{\Delta y'_2} & 0 & 0 \\ \vdots & \vdots & \ddots & \vdots \\ 0 & 0 & 0 & \sqrt{\Delta y'_N} \end{bmatrix} = \begin{bmatrix} \sqrt{\Delta y_1} & 0 & 0 & 0 \\ 0 & \sqrt{\Delta y_2} & 0 & 0 \\ \vdots & \vdots & \ddots & \vdots \\ 0 & 0 & 0 & \sqrt{\Delta y_N} \end{bmatrix} \quad (\text{A5})$$

$$\mathbf{S} = \begin{bmatrix} S_{1,1}(y_1, y'_1; k; f) & S_{1,1}(y_1, y'_2; k; f) & \cdots & S_{1,1}(y_1, y'_N; k; f) \\ S_{1,1}(y_2, y'_1; k; f) & S_{1,1}(y_2, y'_2; k; f) & \cdots & S_{1,1}(y_2, y'_N; k; f) \\ \vdots & \vdots & \ddots & \vdots \\ S_{1,1}(y_N, y'_1; k; f) & S_{1,1}(y_N, y'_2; k; f) & \cdots & S_{1,1}(y_N, y'_N; k; f) \end{bmatrix} \quad (\text{A6})$$

$$\phi^{(n)} = \begin{bmatrix} \phi^{(n)}(y'_1; k; f) \\ \phi^{(n)}(y'_2; k; f) \\ \vdots \\ \phi^{(n)}(y'_N; k; f) \end{bmatrix} = \begin{bmatrix} \phi^{(n)}(y_1; k; f) \\ \phi^{(n)}(y_2; k; f) \\ \vdots \\ \phi^{(n)}(y_N; k; f) \end{bmatrix} \quad (\text{A7})$$

The solution to Eq. (A4) does not produce the correct eigenfunctions because of multiplication of both sides of Eq. (A2) by  $\mathbf{w}$ . Therefore, the eigenfunctions,  $\psi$ , which will be obtained from the solutions are:

$$\psi^{(n)} = \begin{bmatrix} \sqrt{\Delta y'_1} & 0 & 0 & 0 \\ 0 & \sqrt{\Delta y'_2} & 0 & 0 \\ \vdots & \vdots & \ddots & \vdots \\ 0 & 0 & 0 & \sqrt{\Delta y'_N} \end{bmatrix} \begin{bmatrix} \phi^{(n)}(y'_1; k; f) \\ \phi^{(n)}(y'_2; k; f) \\ \vdots \\ \phi^{(n)}(y'_N; k; f) \end{bmatrix} \quad (\text{A8})$$

The correct eigenfunctions can be found by multiplying the solutions with the inverse of the diagonal matrix formed by the square-root of the integrand elements:

$$\phi^{(n)} = \begin{bmatrix} \phi^{(n)}(y_1; k; f) \\ \phi^{(n)}(y_2; k; f) \\ \vdots \\ \phi^{(n)}(y_N; k; f) \end{bmatrix} = \begin{bmatrix} \sqrt{\Delta y_1} & 0 & 0 & 0 \\ 0 & \sqrt{\Delta y_2} & 0 & 0 \\ \vdots & \vdots & \ddots & \vdots \\ 0 & 0 & 0 & \sqrt{\Delta y_N} \end{bmatrix}^{-1} \begin{bmatrix} \psi^{(n)}(y_1; k; f) \\ \psi^{(n)}(y_2; k; f) \\ \vdots \\ \psi^{(n)}(y_N; k; f) \end{bmatrix} \quad (\text{A9})$$

The number of eigenfunctions and eigenvalues depends on the size of the kernel which is the two-point cross-spectral tensor. The kernel is a square matrix of  $(M \times N) \times (M \times N)$ , where

M is the number of velocity components included in the analysis and N is the number of grids, or measurement locations within the field of interest<sup>10,17</sup>. In our experiments, we had 11 probes in the wall-normal direction,  $y$ , spaced logarithmically and only the streamwise velocity component of turbulent velocities was measured. Therefore, the size of the kernel is  $11 \times 11$  for each pair of spanwise Fourier mode,  $k$ , and frequency,  $f$ . Thus, the maximum number of POD modes which can be extracted from the current setting is 11 for each  $k$  and  $f$ .

## ACKNOWLEDGMENTS

The authors would like to thank Peter B. V. Johansson, Faraz Mehdi, Michel Stanislas, Jean-Marc Foucaut, Sebastien Coudert, Jim Kostas, J el Delville and Carine Fourment for their collaboration during the experiments. Unfortunately, the last two members of the team (J. Delville and C. Fourment) passed away in July 2014 because of a traffic accident while returning back to Poitiers from a measurement campaign in Modane. They are greatly missed by the turbulence and flow control community.

The original experimental data were generated by the WALLTURB project. WALLTURB (A European synergy for the assessment of wall turbulence) is funded by the CEC under the 6th framework program (CONTRACT No: AST4-CT-2005-516008). Tutkun’s work is partially financed by the research project DOMT – Developments in Optical Measurement Technologies funded by the Research Council of Norway with project number 231491 under the Frinatek program.

---

\* murat.tutkun@ife.no

<sup>1</sup> J. L. Lumley. The structure of inhomogeneous turbulent flows. In A. M. Yaglom and V. I. Tatarsky, editors, *Atmospheric Turbulence and Radio Wave Propagation*, pages 166–176. Publishing House Nauka, Moscow, USSR, 1967.

<sup>2</sup> W. K. George. A 50-year retrospective and the future. In *Whither Turbulence and Big Data in the 21st Century*, pages 13–43. Springer, 2017.

<sup>3</sup> M. N. Glauser and W. K. George. Orthogonal decomposition of the axisymmetric jet mixing

- layer including azimuthal dependence. In G Comte-Bellot and J. Mathieu, editors, *Advances in Turbulence*, pages 357–366. Springer, Berlin, 1987.
- <sup>4</sup> M. N. Glauser, S. J. Leib, and W. K. George. Coherent structures in the axisymmetric turbulent jet mixing layer. In F. Durst, B. E. Launder, J. H. Lumley, F. W. Schmidt, and J. H. Whitelaw, editors, *Turbulent Shear Flows 5*, pages 134–145. Springer-Verlag, 1985.
- <sup>5</sup> J. H. Citriniti and W. K. George. Reconstruction of the global velocity field in the axisymmetric mixing layer utilizing the proper orthogonal decomposition. *Journal of Fluid Mechanics*, 418:137–166, 2000.
- <sup>6</sup> D. Jung, S. Gamard, and W. K. George. Downstream evolution of the most energetic modes in a turbulent axisymmetric jet at high reynolds number. Part 1. The near-field region. *Journal of Fluid Mechanics*, 514:173–204, 2004.
- <sup>7</sup> S. Gamard, D. Jung, and W. K. George. Downstream evolution of the most energetic modes in a turbulent axisymmetric jet at high reynolds number. Part 2. The far-field region. *Journal of Fluid Mechanics*, 514:205–230, 2004.
- <sup>8</sup> P. B. V. Johansson and W. K. George. The far downstream evolution of the high reynolds number axisymmetric wake behind a disk. Part 2. Slice proper orthogonal decomposition. *Journal of Fluid Mechanics*, 555:387–408, 2006.
- <sup>9</sup> M. Wänström, W. K. George, and K.-E. Meyer. Stereoscopic PIV and POD applied to far turbulent axisymmetric jet. In *AIAA Paper 2006-3368*, 2006.
- <sup>10</sup> M. Tutkun, P. B.V. Johansson, and W. K. George. Three-component vectorial proper orthogonal decomposition of axisymmetric wake behind a disk. *AIAA Journal*, 46(5):1118–1134, May 2008.
- <sup>11</sup> W. K. George. Insight into the dynamics of coherent structures from a proper orthogonal decomposition. In S. Kline, editor, *The Structure of Near Wall Turbulence, Proceedings of Symposium on Near Wall Turbulence*, pages 168–180. Dubrovnik, Yugoslavia, Hemisphere, NY, May 1988.
- <sup>12</sup> H. P. Bakewell and J. L. Lumley. Viscous sublayer and adjacent wall region in turbulent pipe flow. *Physics of Fluids*, 10(9):1880–1889, 1967.
- <sup>13</sup> S. J. Leib, M. N. Glauser, and W. K. George. An application of lumley’s orthogonal decomposition to the axisymmetric turbulent jet mixing layer. In G. L. Patterson and J. L. Zakin, editors, *Proceedings of the 9<sup>th</sup> Rolla Symposium on Turbulence in Fluids*, Rolla, Missouri, 1984. University

of Missouri-Rolla.

- <sup>14</sup> M. N. Glauser. *Coherent Structures in the Axisymmetric Turbulent Jet Mixing Layer*. Ph.D. Dissertation, State University of New York at Buffalo, 1987.
- <sup>15</sup> S. Herzog. *The Large Scale Structure in the Near-Wall Region of Turbulent Pipe Flow*. Ph.d. dissertation, Cornell University, Ithaca, NY, 1986.
- <sup>16</sup> P. Moin and R. D. Moser. Characteristic-eddy decomposition of turbulence in a channel. *Journal of Fluid Mechanics*, 200:471–509, 1989.
- <sup>17</sup> J. Delville. Characterization of the organization in shear layers via the proper orthogonal decomposition. *Applied Scientific Research*, 53:263–281, 1994.
- <sup>18</sup> J. Delville, L. Ukeiley, L. Cordier, J. P. Bonnet, and M. Glauser. Examination of large-scale structures in a turbulent plane mixing layer. Part 1. Proper orthogonal decomposition. *Journal of Fluid Mechanics*, 391:91–122, 1999.
- <sup>19</sup> S. V. Gordeyev and F. O. Thomas. Coherent structure in the turbulent planar jet. Part 1. Extraction of proper orthogonal decomposition eigenmodes and their self-similarity. *Journal of Fluid Mechanics*, 414:145–194, 2000.
- <sup>20</sup> M. O. Iqbal and F. O. Thomas. Coherent structure in a turbulent jet via a vector implementation of the proper orthogonal decomposition. *Journal of Fluid Mechanics*, 571(281-326), 2007.
- <sup>21</sup> R. L. LeBoeuf. *Application of the Proper Orthogonal Decomposition Techniques to an Annular Cascade Flow Field*. Ph.D. Dissertation, State University of New York at Buffalo, 1991.
- <sup>22</sup> L. Ukeiley, M. Glauser, and D. Wick. Downstream evolution of proper orthogonal decomposition eigenfunctions in a lobed mixer. *AIAA Journal*, 31(8):1392–1397, 1993.
- <sup>23</sup> Z. C. Liu, R. J. Adrian, and T. J. Hanratty. Reynolds number similarity of orthogonal decomposition of the outer layer of turbulent wall flow. *Physics of Fluids*, 6(8):2815–2819, 1994.
- <sup>24</sup> L. H. O. Hellström and A. J. Smits. The energetic motions in turbulent pipe flow. *Physics of Fluids*, 26(12), 2014.
- <sup>25</sup> R. Gurka, A. Liberzon, and G. Hetsroni. Pod of vorticity fields: A method for spatial characterization of coherent structures. *International Journal of Heat and Fluid Flow*, 27(3):416–423, 2006.
- <sup>26</sup> Z. Liu, R. J. Adrian, and T. J. Hanratty. Large-scale modes of turbulent channel flow: Transport

- and structure. *Journal of Fluid Mechanics*, 448:53–80, 2001.
- <sup>27</sup> S. C. C. Bailey and A. J. Smits. Experimental investigation of the structure of large- and very large-scale motions in turbulent pipe flow. *Journal of Fluid Mechanics*, 651:339–356, 2010.
- <sup>28</sup> L. H. O. Hellström, B. Ganapathisubramani, and A. J. Smits. The evolution of large-scale motions in turbulent pipe flow. *Journal of Fluid Mechanics*, 779:701–715, 2015.
- <sup>29</sup> JR Baltzer, RJ Adrian, and Xiaohua Wu. Structural organization of large and very large scales in turbulent pipe flow simulation. *Journal of Fluid Mechanics*, 720:236, 2013.
- <sup>30</sup> M. Tutkun, W. K. George, J. Delville, M. Stanislas, P. Johansson, J.-M. Foucaut, and S. Coudert. Two-point correlations in high Reynolds number flat plate turbulent boundary layers. *Journal of Turbulence*, 10(N21):1–23, 2009.
- <sup>31</sup> M. Tutkun, W. K. George, J. M. Foucaut, S. Coudert, M. Stanislas, and J. Delville. In situ calibration of hot wire probes in turbulent flows. *Experiments in Fluids*, 46(4):617–629, 2009.
- <sup>32</sup> S. Coudert, J.-M. Foucaut, J. Kostas, M. Stanislas, P. Braud, C. Fourment, J. Delville, M. Tutkun, F. Mehdi, P. Johansson, and W. K. George. Double large field stereoscopic PIV in a high Reynolds number turbulent boundary layer. *Experiments in Fluids*, 50(1):1–12, 2011.
- <sup>33</sup> J. Carlier and M. Stanislas. Experimental study of eddy structures in a turbulent boundary layer using particle image velocimetry. *Journal of Fluid Mechanics*, 535:143–188, 2005.
- <sup>34</sup> M. Stanislas, L. Perret, and J.-M. Foucaut. Vortical structures in the turbulent boundary layer: a possible route to a universal representation. *Journal of Fluid Mechanics*, 602:327–382, 2008.
- <sup>35</sup> S. H. Woodward. *Progress Toward Massively Parallel Thermal Anemometry System*. M.Sc. Thesis, State University of New York at Buffalo, 2001.
- <sup>36</sup> S. H. Woodward, D. Ewing, and L. Jernqvist. Anemometer system review. In *In Sixth Annual Symposium on Thermal Anemometry*, Melbourne, Australia, Jan. 8-10 2001.
- <sup>37</sup> W. K. George<sup>2</sup> suggests calling this the 'Lumley integral' instead of the more customary 'POD integral', since the solutions are proper only for the inhomogeneous directions.
- <sup>38</sup> P. Holmes, J. H. Lumley, and G. Berkooz. *Turbulence, Coherent Structures, Dynamical Systems and Symmetry*. Cambridge University Press, U.K., 1996.
- <sup>39</sup> W. K. George and L. Castillo. Zero pressure gradient turbulent boundary layer. *Applied Mechanics Review*, 50(12):689–729, 1997.

- <sup>40</sup> M. Wosnik, L. Castillo, and W. K. George. A theory for turbulent pipe and channel flows. *Journal of Fluid Mechanics*, 421:115–145, 2000.
- <sup>41</sup> R. F. Blackwelder and L. S. G. Kovaszny. Time scales and correlations in a turbulent boundary layer. *Physics of Fluids*, 15(9):1545–1554, 1972.
- <sup>42</sup> M. Guala, S. E. Himmema, and R. J. Adrian. Large-scale and very-large-scale motions in turbulent pipe flow. *Journal of Fluid Mechanics*, 554:521–542, 2006.
- <sup>43</sup> J. P. Monty, J. A. Stewart, R. C. Williams, and M. S. Chong. Large-scale features in turbulent pipe and channel flows. *Journal of Fluid Mechanics*, 589:147–156, 2007.
- <sup>44</sup> K. C. Kim and R. J. Adrian. Very large-scale motion in the outer layer. *Physics of Fluids*, 11(2):417–422, 1999.
- <sup>45</sup> J. C. del Álamo and J. Jimenez. Spectra of the very large anisotropic scales in turbulent channels. *Physics of Fluids*, 15(6):L41–L44, 2003.
- <sup>46</sup> B. J. Balakumar and R. J. Adrian. Large- and very-large-scale motions in channel and boundary-layer flows. *Philosophical Transactions of the Royal Society A*, 365:665–681, 2007.
- <sup>47</sup> R. J. Adrian. Hairpin vortex organization in wall turbulence. *Physics of Fluids*, 19(041301):1–16, 2007.
- <sup>48</sup> A. A. Townsend. *The Structure of Turbulent Shear Flow*. Cambridge University Press, United Kingdom, second edition, 1976.
- <sup>49</sup> R. F. Blackwelder and R. E. Kaplan. On the wall structure of the turbulent boundary layer. *Journal of Fluid Mechanics*, 76:89–112, 1976.
- <sup>50</sup> R. Mathis, N. Hutchins, and I. Marusic. Large-scale amplitude modulation of the small-scale structures in turbulent boundary layers. *Journal of Fluid Mechanics*, 628:311–337, 2009.